

How Insoluble Inclusions and Intersecting Layers Affect the Leaching Process within Potash Seams

Svenja Steding¹, Thomas Kempka¹, and Michael Kühn²

¹GFZ German Research Centre for Geosciences

²Helmholtz Centre Potsdam - GFZ German Research Centre for Geosciences

November 23, 2022

Abstract

Potash seams are a valuable resource containing several economically interesting, but also highly soluble minerals. One of the major safety risks for subsurface mining operations is the formation of leaching zones which is controlled by the mineralogical composition and the dissolution rate of the salt rock. In the present study, a reactive transport model including mineral-specific, saturation-dependent dissolution rates is used to examine the influence of insoluble inclusions and intersecting layers. For that purpose, a scenario-analysis is carried out considering different rock distributions within a carnallite-bearing potash seam. The results show that the validity of the dimensionless Damköhler number (Da) decreases if insoluble areas become broader and more inclined. However, with regard to the growth rate of the leaching zone, the exact distribution of insoluble inclusions is of minor importance. While reaction-dominated systems ($Da < 1$) are not affected by these at all, the dissolution front of transport-dominated systems ($Da > 1$) advances more slowly compared to homogeneous potash seams. However, the ratio of permeated rock in vertical direction becomes higher. Accordingly, heterogeneous potash seams are beneficial with regard to risk assessment as long as the mechanical stability of the leaching zone is given. For determining dissolution rates, saturation-dependency should always be considered as it increases the hazard potential in the long-term. Literature data confirm the simulation results and indicate that most systems in nature are transport-dominated. To investigate the effects of mineral heterogeneity in further detail, more experimental data on the dissolution kinetics of potash salt are required.

1 **How Insoluble Inclusions and Intersecting Layers Affect the Leaching Process within**
2 **Potash Seams**

3 **Svenja Steding^{1,2}, Thomas Kempka^{1,2}, and Michael Kühn^{1,2}**

4 ¹GFZ German Research Centre for Geosciences, Potsdam, Germany.

5 ²University of Potsdam, Institute of Geosciences, Potsdam, Germany.

6 Corresponding author: Svenja Steding (ssteding@gfz-potsdam.de)

7 **Key Points:**

- 8 • Insoluble inclusions and interlayers in potash seams slow down the leaching zone growth
9 in case of transport-dominated systems.
- 10 • Distribution of inclusions is of minor importance, while inclinations of intersecting layers
11 are more relevant for risk assessment.
- 12 • Saturation-dependent dissolution rates change the leaching zone shape and should be
13 considered for further scenario analyses.
14

15 **Abstract**

16 Potash seams are a valuable resource containing several economically interesting, but also highly
17 soluble minerals. One of the major safety risks for subsurface mining operations is the formation
18 of leaching zones which is controlled by the mineralogical composition and the dissolution rate
19 of the salt rock. In the present study, a reactive transport model including mineral-specific,
20 saturation-dependent dissolution rates is used to examine the influence of insoluble inclusions
21 and intersecting layers. For that purpose, a scenario-analysis is carried out considering different
22 rock distributions within a carnallite-bearing potash seam. The results show that the validity of
23 the dimensionless Damköhler number (Da) decreases if insoluble areas become broader and
24 more inclined. However, with regard to the growth rate of the leaching zone, the exact
25 distribution of insoluble inclusions is of minor importance. While reaction-dominated systems
26 ($Da < 1$) are not affected by these at all, the dissolution front of transport-dominated systems (Da
27 > 1) advances more slowly compared to homogeneous potash seams. However, the ratio of
28 permeated rock in vertical direction becomes higher. Accordingly, heterogeneous potash seams
29 are beneficial with regard to risk assessment as long as the mechanical stability of the leaching
30 zone is given. For determining dissolution rates, saturation-dependency should always be
31 considered as it increases the hazard potential in the long-term. Literature data confirm the
32 simulation results and indicate that most systems in nature are transport-dominated. To
33 investigate the effects of mineral heterogeneity in further detail, more experimental data on the
34 dissolution kinetics of potash salt are required.

35 **1 Introduction**

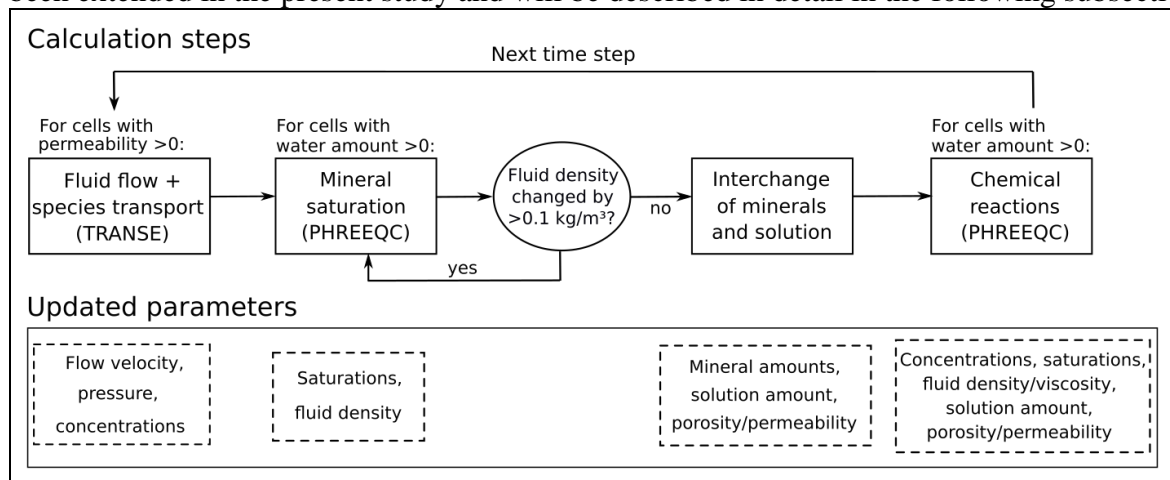
36 The role of potash seams within salt deposits can be viewed from different perspectives:
37 on the one hand, they are a valuable resource that has been mined for many decades, while on the
38 other hand, they represent a potential risk for technical caverns and subsurface waste repositories
39 (Warren, 2017). However, both perspectives have in common that the formation of leaching
40 zones within potash seams is considered as highly critical. Due to the increased solubility of
41 potash salt, leaching zones can grow relatively fast and jeopardise the integrity and mechanical
42 stability of mines or technical caverns (Prugger & Prugger, 1991; Boys, 1993; Keime et al.,
43 2012; Mengel et al., 2012). In order to describe their temporal and spatial evolution, reactive
44 transport models are required (Dijk & Berkowitz, 2000). Steding et al. (2021) showed that the
45 Péclet (Pe) and Damköhler (Da) numbers represent useful indicators to evaluate growth rates,
46 shapes and mineralogical compositions of leaching zones within potash seams, providing a basis
47 to estimate the hazard potential. However, so far only homogeneous potash seams have been
48 investigated. Studies for rock salt and other minerals indicate that local variations in the
49 proportion of potash minerals as well as inclusions or layers of insoluble materials may have a
50 significant influence on shapes and growth rates (Thoms & Gehle, 1999; Li et al., 2018; Jinlong
51 et al., 2020; Liu et al., 2017; Wei et al., 2019).

52 This study focusses on how heterogeneities in the form of inclusions and intersecting
53 layers of pure halite (further referred to as halitic areas) affect the evolution of leaching zones
54 within potash seams. The reactive transport model presented by Steding et al. (2021) is used to
55 perform a scenario analysis under density-driven flow conditions. Six different mineral
56 distributions are investigated with halitic areas ranging from several small inclusions to one
57 continuous layer. Inclined layers are examined as well, since these may cause an asymmetric
58 expansion of leaching zones (Fokker, 1995). The penetrating solution is assumed to be NaCl-

59 saturated, i.e. halitic areas are basically insoluble, what makes them acting as impermeable
 60 barriers. This is expected to considerably change the hydrodynamic conditions and saturation
 61 distribution within leaching zones. To quantify these effects, the temporal and spatial leaching
 62 zone evolutions are analysed and compared to that of a homogeneous potash seam. Furthermore,
 63 the maximum dissolution rate of potash salt is varied by two orders of magnitude to identify the
 64 differences between reaction-dominated ($Da < 1$) and transport-dominated ($Da > 1$) systems.
 65 Additionally, the interchange approach (Steding et al., 2021) was extended to include saturation-
 66 dependent dissolution rates. The aim of our study is to find out how insoluble layers and
 67 inclusions influence the evolution and hazard potential of leaching zones, and if a classification
 68 based on the Pe and Da numbers is still possible in case of heterogeneous mineral distributions.

69 2 Materials and Methods

70 The concept of the applied reactive transport model is shown in Figure 1. Each
 71 simulation time step starts with the solution of the partial differential equations for fluid flow and
 72 transport of chemical species using the TRANSE Simulation Environment (TRANSE)
 73 (Kempka, 2020). TRANSE is coupled with the geochemical reaction module PHREEQC
 74 (Parkhurst & Appelo, 2013) applied in combination with the THEREDA database (Altmaier et
 75 al., 2011). In the second calculation step, PHREEQC is used to update fluid densities and
 76 mineral saturations after transport. After that, a step called „interchange“ is performed which
 77 describes the dissolution of minerals from (nearly) dry into permeated cells and allows the
 78 dissolution front to move forward (Steding et al., 2021). The terms „dry“ and „permeated“ are
 79 used in view of the fluid saturation in the pore space, while the term „saturated“ refers to the
 80 chemical equilibration of the solution with respect to salt minerals. In the final calculation step,
 81 the chemical reactions resulting from transport and interchange are determined using PHREEQC.
 82 Thereby, thermodynamic equilibrium is assumed within each cell. The updated concentrations
 83 and fluid properties, such as density and viscosity, are then transferred back to TRANSE to
 84 calculate flow and transport in the next simulation time step (Figure 1). More details on this
 85 procedure are presented in Steding et al. (2021). The interchange of minerals and solution has
 86 been extended in the present study and will be described in detail in the following subsection.



87 **Figure 1.** Flow sheet of the coupled reactive transport model: calculations undertaken at each
 88 simulation time step and associated output parameters (modified from Steding et al., 2021).

89 2.1 Extended interchange approach

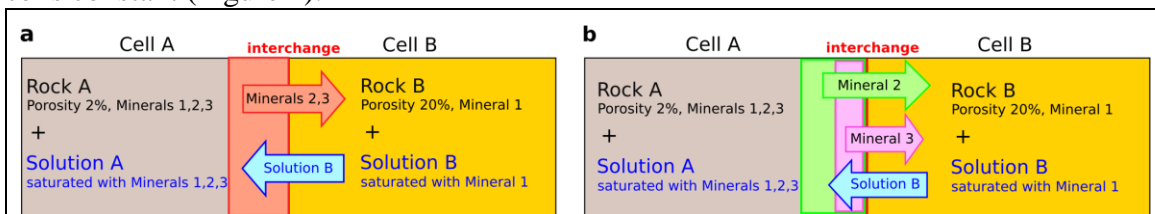
90 In Steding et al. (2021), constant dissolution rates were used to calculate the
 91 interchange of salt minerals. However, it is known that close to equilibrium the
 92 dissolution rates decrease considerably (Durie & Jessen, 1964; Röhr, 1981; Palandri &
 93 Kharaka, 2004). Based on the results of Alkattan et al. (1997), a linear saturation-
 94 dependency is assumed:

$$95 \text{ rate} = k_{max} \cdot (1 - \Omega) \quad \text{with } \Omega = Q/K = 10^{SI} \quad (1)$$

96 and k_{max} (cm/s) as dissolution rate in an infinitely dilute solution. Q is the activity product
 97 and K the equilibrium constant. The saturation index SI (-) results from $\log(Q/K)$. Since
 98 the maximum dissolution rate k_{max} as well as the saturation state vary across minerals, an
 99 average dissolution rate for the potash seam (Figure 2a) is not applicable here. Instead,
 100 the dissolution rate rate (cm/s) and the amount of minerals dissolved into an adjacent cell
 101 Min_{sol} (mol) need to be calculated individually for each mineral (Figure 2b). Thereby,
 102 rate always refers to the saturation state of the solution the mineral is dissolved into.
 103 Between Cell A and Cell B the amount of interchanged mineral n is calculated by
 104 equation (2):

$$105 Min_{sol,n} = rate_n \cdot Min_{A,n}/di \cdot (\Phi_B - \Phi_A)/(1 - \Phi_A) \cdot dt \quad (2)$$

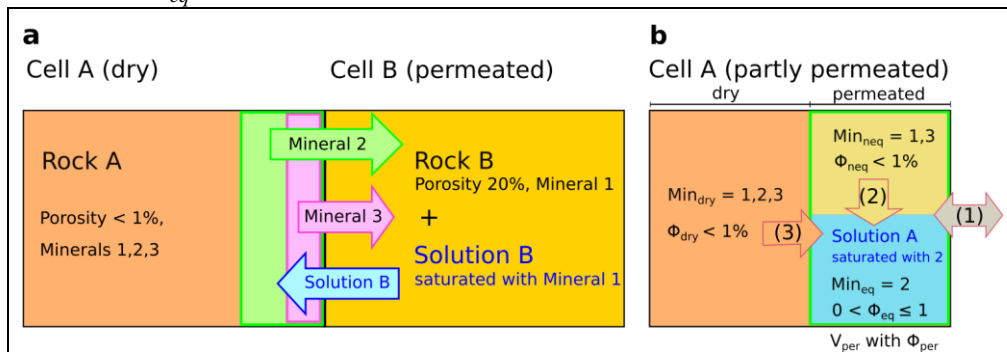
106 The amount of mineral n present in Cell A, $Min_{A,n}$ (mol), divided by the cell diameter
 107 perpendicular to the dissolution front di (cm) gives the affected amount of mineral n if
 108 the width of 1 cm is dissolved from Cell A. To take into account the contact area between
 109 the rock in Cell A and the solution in Cell B, this amount is multiplied with the porosity
 110 difference between both cells ($\Phi_B - \Phi_A$) and divided by the volume fraction of the rock in
 111 Cell A ($1 - \Phi_A$). If $\Phi_A \geq \Phi_B$, the interchange is zero, i.e. minerals can only be dissolved into
 112 adjacent cells with higher porosity. dt (s) is the length of the simulation time step. If the
 113 solution in Cell B is already saturated with respect to n , $rate_n$ becomes zero and the
 114 mineral is not dissolved. The interchange takes place at each interface between two cells
 115 within the model. The volumes of all minerals dissolved at one interface are cumulated to
 116 determine the amount of solution that is transferred in return to keep the volume of both
 117 cells constant (Figure 2).



118 **Figure 2.** Sketch of the interchange approach with (a) constant and (b) variable
 119 dissolution rates. A defined amount of each mineral according to equation (2) is dissolved
 120 from a cell with low porosity (Cell A) into an adjacent cell with higher porosity (Cell B).
 121 These amounts are cumulated and the solution is transferred into the cell with lower
 122 porosity to fill the newly formed pore space (modified from Steding et al., 2021).

123 At the dissolution front, the interchange approach enables originally dry cells to
 124 receive solution for the first time from an adjacent cell (Figure 3a). The solution needs to
 125 be undersaturated with at least one of the minerals from the dry rock, otherwise no

126 interchange takes place. Newly permeated cells are divided into a permeated and a dry
 127 sub-cell to avoid an immediate drying out due to high solid-fluid-ratios (Figure 3b). In
 128 case of constant dissolution rates, all minerals in the permeated part were assumed to be
 129 in equilibrium with the solution of the cell, while minerals in the dry part are not
 130 considered in the subsequent calculation of chemical reactions (Steding et al., 2021).
 131 However, as shown in Figure 3a, the varying dissolution rates challenge the identification
 132 of a clear borderline between dry and permeated or equilibrated and non-equilibrated
 133 parts, respectively. In can be seen that Mineral 2 has the highest dissolution rate, and
 134 therefore limits the region of increased porosity where mineral solution occurs (green).
 135 Within this region, it is reasonable to equilibrate the solution with regard to Mineral 2.
 136 However, Mineral 3 has a lower dissolution rate, and can therefore only be equilibrated
 137 with the solution in the pink subregion. Following this reasoning, one would end up with
 138 an additional subregion for each mineral, which is of course not practical. Instead, the
 139 permeated part within each cell is split up into minerals that are in equilibrium with the
 140 solution (equilibrated minerals Min_{eq}) and such that are not (non-equilibrated minerals
 141 Min_{neq}) (Figure 3b). Thereby, the volume of the permeated part V_{per} is determined by the
 142 most soluble mineral (Mineral 2, green area). Outside of this area, the salt rock is still dry
 143 and the composition Min_{dry} corresponds to the originally unaffected potash seam. In
 144 contrast, minerals within the permeated area V_{per} are surrounded by solution, whereby it
 145 is not yet in equilibrium with all minerals. Minerals that remain undissolved during the
 146 interchange due to their lower dissolution rates (Mineral 1 and parts of Mineral 3 within
 147 the green area, Figure 3a) are assigned to the non-equilibrated minerals Min_{neq} . In
 148 contrast, precipitations from Solution B belong to the minerals equilibrated with the
 149 solution Min_{eq} .



150 **Figure 3.** Sketch of the interchange at the dissolution front (a) resulting in a partly
 151 permeated cell (b). The permeated part V_{per} contains minerals Min_{eq} that are in
 152 equilibrium with Solution A and minerals Min_{neq} that are not. Besides interchange with
 153 adjacent cells (1), the internal dissolution of non-equilibrated minerals (2) and dry
 154 minerals (3) is considered following equations (2), (4) and (5) (modified from Steding et
 155 al., 2021).

156 In case of partly permeated cells, three different types of dissolution can occur
 157 (Figure 3b): the first one is the interchange with (fully permeated) adjacent
 158 according to Equation (2). For this, all three mineral compositions Min_{dry} , Min_{eq} and
 159 Min_{neq} are added up to determine Min_A . Φ_A is the average porosity of the cell calculated
 160 from the volume of Min_A related to the cell volume. If the partly permeated cell shows a
 161 higher average porosity than the fully permeated one, the interchange of minerals is

162 possible in reverse direction as well. The dissolved amount of each mineral is split among
 163 Min_{dry} , Min_{eq} and Min_{neq} according to their contribution to the total amount of this
 164 mineral. The solution transferred in return is mixed with the pre-existing solution in the
 165 permeated part. The chemical reactions resulting from the mixing and the following
 166 equilibration with Min_{eq} are determined after the interchange (Figure 1).

167 In addition to the interchange, internal dissolution processes within cells
 168 containing dry (Min_{dry}) or non-equilibrated (Min_{neq}) minerals need to be taken into
 169 account (Figure 3b). The interface area between a dry part and the adjacent permeated
 170 part(s) is assumed to be constant over time. At the beginning, when the cell is completely
 171 dry, the only adjacent permeated area is the neighbour cell and dry minerals can only be
 172 dissolved via interchange. Accordingly, the interface area is the interface between both
 173 cells, which is the cell width multiplied by its height. As V_{per} increases, Min_{dry} makes up a
 174 smaller part of the total mineral amount within the partly permeated cell and its
 175 interchange amount decreases. At the same time, the interface area between the dry and
 176 permeated parts within the partly permeated cell increases enhancing the internal
 177 dissolution of dry minerals. To account for that, the permeation state of the cell S_{per} (-) is
 178 calculated referring to the volume of the permeated part V_{per} in relation to the cell volume
 179 V_{cell} :

$$180 \quad S_{per} = V_{per}/V_{cell} \quad (3)$$

181 The higher S_{per} , the more of the dry rock is dissolved into the solution of its own
 182 cell (by internal dissolution) instead of the adjacent cell (by interchange). Equation (4) is
 183 used to determine the amount of mineral n dissolved from Min_{dry} into the solution within
 184 the permeated part:

$$185 \quad Min_{sol,dry,n} = rate_n \cdot Min_{dry,n} / (di \cdot (1 - S_{per})) \cdot \Phi_{per} \cdot S_{per} \cdot dt \cdot \quad (4)$$

186 Generally, equation (4) is identical to equation (2), but multiplied by the permeation state
 187 S_{per} . $rate$ is calculated from the saturation state within the partly permeated cell using
 188 equation (1). In order to determine the affected amount of mineral n if a width of 1 cm of
 189 the dry part is dissolved, the present amount, $Min_{dry,n}$ (mol), is divided by the diameter of
 190 the dry part perpendicular to the dissolution front. Therefore, the cell diameter di (cm) is
 191 now multiplied by the volume ratio of the dry part ($1 - S_{per}$). The porosity within the dry
 192 part is nearly zero, simplifying the term $(\Phi_B - \Phi_A)/(1 - \Phi_A)$ in equation (2) to Φ_B , which
 193 equals the average porosity of the permeated part Φ_{per} . The dissolved amount of each
 194 mineral $Min_{sol,dry}$ is added to Min_{eq} . The same applies to precipitations resulting from the
 195 equilibration after the interchange (Figure 1). Similar to the interchange of dry minerals,
 196 the highest dissolution rate according to equation (1) determines the volume that is newly
 197 added to the permeated part V_{per} (Figure 3). For minerals with lower dissolution rates, the
 198 difference between the amount within this volume and the dissolved amount is added to
 199 Min_{neq} .

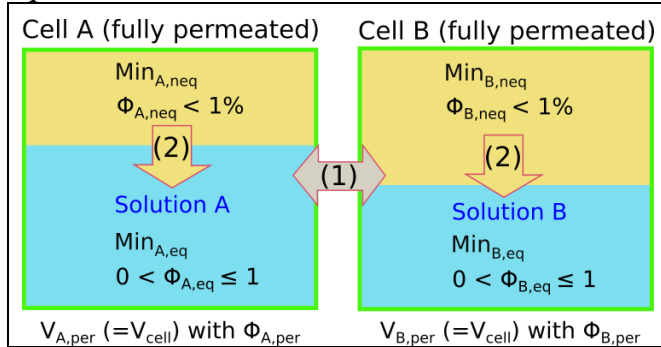
200 Finally, the internal dissolution of non-equilibrated minerals (Min_{neq}) has to be
 201 taken into account (Figure 3b). These minerals belong to the permeated part of a cell and
 202 are already surrounded by solution. However, when the area is permeated for the first
 203 time, their dissolution rate is too low to dissolve all minerals. Basically, there are two
 204 possible reasons for this: either the maximum dissolution rate k_{max} is (much) lower than

205 that of the other minerals, or the solution is already (nearly) saturated with these. In the
 206 latter case, one could add them to Min_{eq} without changing the solution or rock
 207 composition of the permeated part. However, the solution composition changes over time
 208 and originally saturated minerals may become undersaturated. In this case, an immediate
 209 equilibration could induce errors because the lower dissolution rates would be neglected.
 210 To account for the variation of dissolution rates, Min_{neq} is added stepwise to the solution.
 211 The dissolved amount $Min_{sol,neq}$ (mol) of each mineral is determined by equation (5):

$$\begin{aligned}
 212 \quad Min_{sol,neq,n} &= rate_n \cdot Min_{neq,n} / V_{neq} \cdot contact_area \cdot dt \\
 213 \quad &= rate_n \cdot Min_{neq,n} / V_{neq} \cdot factor \cdot di \cdot 1m \cdot \Phi_{eq} \cdot S_{per} \cdot dt \quad (5)
 \end{aligned}$$

214 The rate law is similar to those used for interchange (equation 2) and internal
 215 dissolution of dry minerals (equation 4). Again, $rate$ (cm/s) is calculated from the
 216 saturation state within the partly permeated cell according to equation (1). Min_{neq} (mol)
 217 divided by the volume of the non-equilibrated minerals V_{neq} (cm³) and multiplied by the
 218 contact area between non-equilibrated minerals and solution (cm²), what gives the
 219 amount of mineral n if a width of 1 cm of the non-equilibrated minerals is dissolved. V_{neq}
 220 is calculated from the mineral amounts and densities in Min_{neq} , neglecting small
 221 porosities. However, the contact area between non-equilibrated minerals and solution is
 222 hard to determine, since the pore structure and spatial arrangement of the different
 223 minerals in the original rock are unknown. Therefore, a variable called $factor$ (-) is
 224 introduced. If it is set to 1, a rectangular contact area similar to that between Min_{dry} and
 225 the solution (equation 4) is assumed. This can be seen as a minimum value. If
 226 precipitations do not block the access to Min_{neq} , the contact area to the solution flowing
 227 between the non-equilibrated minerals should be several times higher. Therefore, it can
 228 make sense to simplify the approach and to directly add Min_{neq} to Min_{eq} . In this case, it is
 229 assumed that the contact area is large enough to immediately equilibrate minerals and
 230 solution within an originally dry volume as soon as the first mineral has been dissolved
 231 from it. However, this is only realistic if the maximum mineral dissolution rates do not
 232 vary by several orders of magnitude. Furthermore, the first mineral dissolved should
 233 make up more than a few vol.% of the dry rock in order to create a sufficiently large
 234 contact area. If this is not the case, the internal dissolution of non-equilibrated minerals
 235 has to be considered. For some minerals, this may take much longer than the permeation
 236 of the cell, i.e. fully permeated cells can still contain non-equilibrated minerals (Figure
 237 4). For the interchange according to equation (2), Min_{eq} and Min_{neq} are added up to

238 determine Min_A and Φ_A is defined as the average porosity of equilibrated and non-
 239 equilibrated areas.



240 **Figure 4.** Fully permeated cells can still contain non-equilibrated minerals due to their
 241 lower dissolution rates. Internal dissolution (2) within a cell reduces the amount of non-
 242 equilibrated minerals; additionally they are considered for interchange (1). The average
 243 porosity of the permeated part Φ_{per} corresponds to the average porosity of the cell and is
 244 used for interchange as well as for flow and transport calculations.

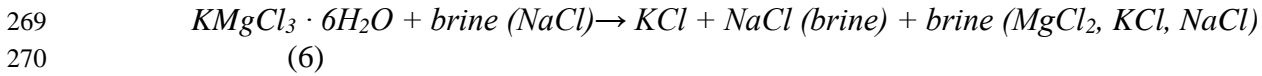
245 Generally, it is assumed that minerals belonging to Min_{eq} are first dissolved if an
 246 undersaturation occurs. As a result, the interchange or internal dissolution of minerals
 247 present in Min_{eq} is not possible. Chemical reactions resulting from the processes
 248 described above are determined in the final calculation step of the simulation (Figure 1).
 249 Thereby, thermodynamic equilibrium is assumed in every cell. The average porosity of
 250 the cell is always used in the flow and transport simulation step.

251 2.2 Scenario analyses

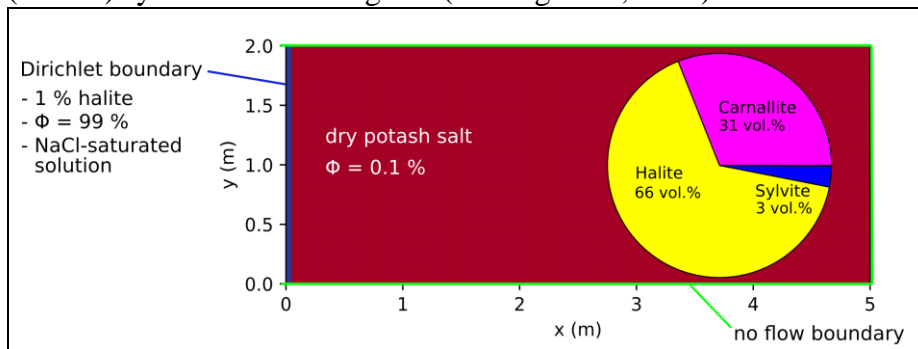
252 In order to study the influence of heterogeneities, the leaching process of a
 253 carnallite-bearing potash seam containing halite layers or inclusions is simulated.
 254 Carnallite is a very common, globally occurring potash salt with carnallite ratios of up
 255 to >80 wt.%. Its leaching behaviour for homogeneous rock compositions has been
 256 studied by Steding et al. (2021), and it was found that the evolution of the leaching zone
 257 can be described based on the Péclet (Pe) and Damköhler (Da) numbers. Most common
 258 and also most critical in the short term with regard to hazard potential are transport- and
 259 advection-dominated systems ($Da > 1$ and $Pe > 2$), resulting from porosities $\geq 10\%$ and
 260 dissolution rates $\geq 10^{-5}$ cm/s. However, reaction- and advection-dominated systems ($Da <$
 261 1 and $Pe > 2$) can be more critical in the long term, since flow barrier formation does not
 262 occur. Both cases are investigated in this study to identify possible differences in the
 263 effect of heterogeneities.

264 In all scenarios, the carnallite-bearing potash seam consists of 25 wt.% carnallite,
 265 72 wt.% halite and 3 wt.% sylvite, corresponding to the volume fractions shown in Figure
 266 5. If it gets into contact with NaCl brine, carnallite is always dissolved first causing a

267 precipitation of sylvite and halite (Koch & Vogel, 1980). Equation (6) gives the overall
 268 reaction:



271 According to Steding et al. (2021), 25 wt.% carnallite are sufficiently high to
 272 produce Péclet numbers >2 and low enough to ensure that Darcy flow is maintained
 273 while the mechanical stability of the porous leaching zone is not compromised. The
 274 densities and dissolution properties of the minerals are provided in Table 1. The
 275 dissolution rate k_{max} strongly depends on the hydrodynamic boundary conditions: it
 276 increases with flow velocity (Yang et al., 2017), and reaches values under turbulent flow
 277 conditions that are at least one order of magnitude higher than for laminar flow (Durie &
 278 Jessen, 1964; Alkattan et al., 1997). This is due to most salt minerals showing transport-
 279 controlled dissolution behaviour, i.e. k_{max} is controlled by the thickness of the diffusive
 280 boundary layer at the mineral surface (Hoppe & Winkler, 1974; Alkattan et al., 1997; De
 281 Baere et al., 2016). The boundary layer thickness, and consequently k_{max} , depend on the
 282 flow velocity, diffusion coefficients and surface roughness (Dreybrodt & Buhmann,
 283 1991; Raines & Dewers, 1997; Ahoulou et al., 2020; Dutka et al., 2020). Based on the
 284 values of Röhr (1981), an average k_{max} of $5 \cdot 10^{-4}$ cm/s is applied to all three minerals in
 285 Table 1. However, this is an upper value since it refers to convection in open cavities. It
 286 can be expected that convection within a porous leaching zone results in smaller flow
 287 velocities, and therefore in smaller dissolution rates. Accordingly, a second k_{max} of $5 \cdot 10^{-6}$
 288 cm/s is taken into account to ensure that both, transport- ($Da > 1$) and reaction-dominated
 289 ($Da < 1$) systems are investigated (Steding et al., 2021).



290 **Figure 5.** Initial and boundary conditions: the inflow region is prescribed by a Dirichlet
 291 boundary (blue line); all other boundaries are impermeable (green lines); the models are

292 initialised as dry with homogeneous potash salt (red, mineralogical composition shown)
 293 and halite inclusions according to Figure 6 (modified from Steding et al., 2021).

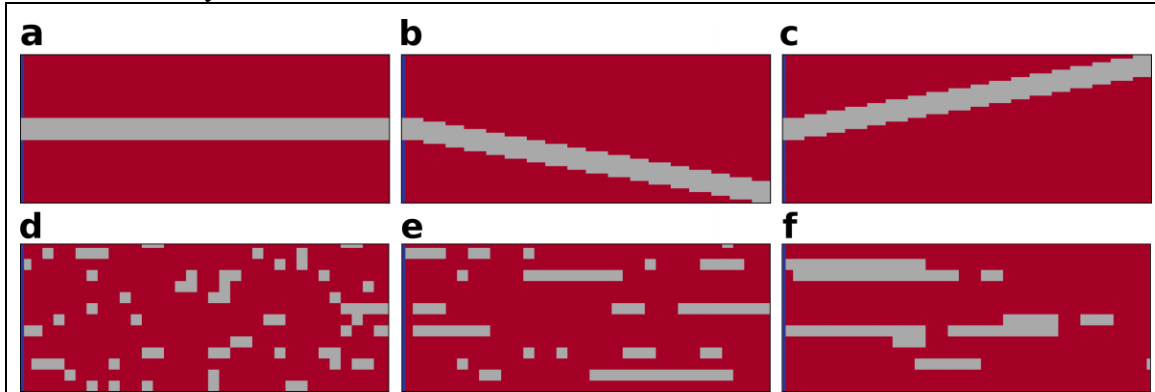
294 **Table 1.** Potash salt mineral densities and dissolution properties (modified from Steding
 295 et al., 2021).

Mineral	Density (kg/m ³)	Reaction equation (dissolution)	Log K
Carnallite	1600	$\text{KMgCl}_3 \cdot 6\text{H}_2\text{O} \rightarrow 3\text{Cl}^- + 6\text{H}_2\text{O} + \text{K}^+ + \text{Mg}^{2+}$	4.33
Halite	2170	$\text{NaCl} \rightarrow \text{Cl}^- + \text{Na}^+$	1.586
Sylvite	1990	$\text{KCl} \rightarrow \text{Cl}^- + \text{K}^+$	0.915

296 The 2D model height is 2 m, representing the typical thickness of potash seams in
 297 Germany, while the model width is 5 m with a discretization of 101 x 41 cells (Figure 5).
 298 At the start of the simulation, the entire model consists of dry potash salt with a porosity
 299 of 0.1%. Natural caverns and leaching zones are commonly formed in the vicinity of
 300 tectonic fault systems which enable fluid migration (Höntzsch & Zeibig, 2014). Due to
 301 the fact that the ascending solution has to cross several rock salt layers before it reaches
 302 the potash seam, it is usually NaCl-saturated. To represent such a fault zone, a Dirichlet
 303 boundary condition is used (Figure 5). It maintains a constant solution composition and
 304 porosity at the left model boundary, assuming a high fluid and mineral exchange rate
 305 within the fault zone. The other boundaries are considered as impermeable without any
 306 pre-defined pressure gradient applied. The 2D model makes use of the horizontally
 307 symmetric expansion of leaching zones to be expected if a potash seam has the same
 308 composition in both horizontal directions. Seen from the fault zone, the starting point of
 309 the leaching process, only one direction is simulated by taking advantage of the
 310 symmetry to reduce the required computational time.

311 Generally, the local variation of mineral proportions within carnallite-bearing
 312 potash seams is relatively low. However, heterogeneities in the form of inclusions or
 313 intersecting layers of (nearly) pure halite are a regular occurrence. Due to the fact that the
 314 solution leaving the fault zone is already NaCl-saturated, halite is usually not dissolved
 315 from the potash seam (Koch & Vogel, 1980; Steding et al., 2021). Accordingly, areas of
 316 pure halite act as barriers and affect the flow field of the leaching zone. To investigate
 317 their influence on the leaching zone evolution and its hazard potential, six different
 318 distributions are considered. As shown in Figure 6, the first three represent a potash seam
 319 (red) with intersecting layers of halite (grey). These layers are 30 cm thick and show
 320 inclinations of 0° or ±10°, respectively (Figures 6a-c). To ensure that boundary
 321 conditions are comparable, the layers always start at the same height at the centre of the
 322 fault zone. In the other three cases, the potash seam contains halite inclusions ranging
 323 from 10 cm x 10 cm (Figure 6d) to nearly continuous, horizontal layers (Figure 6f). Their
 324 distribution is created with GSTools (Müller & Schüller, 2021) using correlation lengths
 325 of 2:1, 17:0.5 and 34:1 in horizontal direction. In all six cases, the halitic area makes up
 326 between 13% and 15% of the potash seam and the surrounding potash salt is

327 homogeneous with the composition shown in Figure 5. For comparison, an additional
 328 case without any halitic areas is considered.



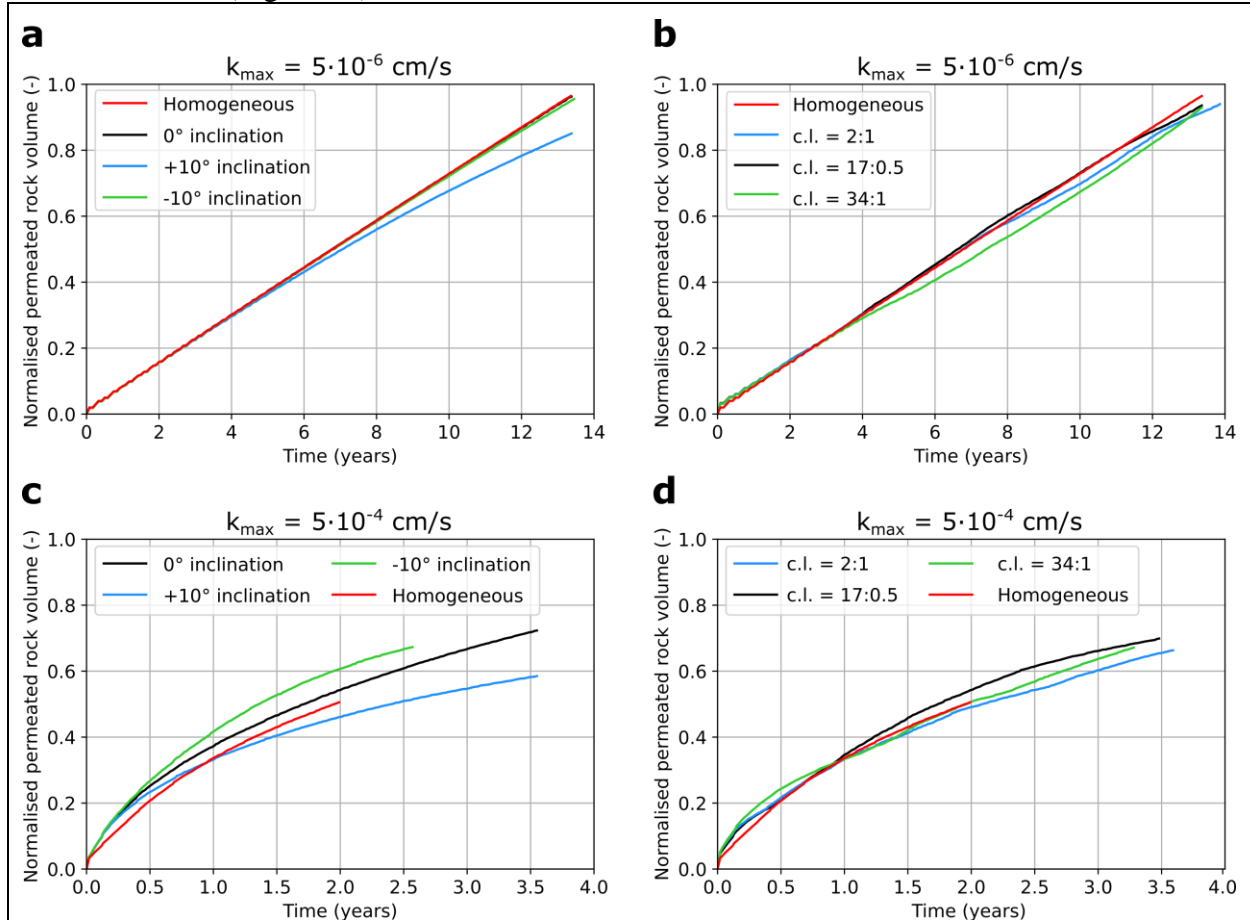
329 **Figure 6.** Heterogeneous rock distributions examined: The homogeneous potash salt
 330 (red) shown in Figure 5 is veined by layers with (a) 0° , (b) $+10^\circ$, (c) -10° inclination or
 331 inclusions of pure halite with correlation lengths of (d) 2:1, (e) 17:0.5 and (f) 34:1 that
 332 make up 13-15% of the potash seam.

333 Following equation (6) and the volume ratios presented in Figure 5, maximum
 334 final porosities of around 30% can be expected (Steding et al., 2021). The porosity-
 335 permeability relationship by Xie et al. (2011) is used with a maximum permeability of
 336 $2 \cdot 10^{-11} \text{ m}^2$ ($\approx 30\%$ porosity) being applied. Since carnallite is dissolved first and making
 337 up $>30\%$ of the rock volume, a relatively large contact area between the solution and
 338 remaining minerals, sylvite and halite, can be assumed. Both minerals show the same
 339 maximum dissolution rate k_{max} as carnallite, facilitating a quick equilibration in case of
 340 under-saturations. Therefore, non-equilibrated minerals are neglected in this study.
 341 Instead, sylvite and halite are immediately added to the equilibrated part Min_{eq} as soon as
 342 the carnallite in their surroundings is dissolved. The diffusion coefficients of all four
 343 transported species Na^+ , Cl^- , K^+ and Mg^{2+} are assumed to be equal and constant: an
 344 average value of $D_f = 1.5 \cdot 10^{-9} \text{ m}^2/\text{s}$ is chosen based on Yuan-Hui and Gregory (1974).
 345 The fluid compressibility is set to $c_f = 4.6 \cdot 10^{-10} \text{ 1/Pa}$. Since temperature differences are
 346 negligible for a model height of 2 m, all simulations are undertaken at isothermal
 347 conditions at a temperature of 25°C . Accordingly, the density-driven convective flow
 348 exclusively occurs due to dissolution and precipitation processes. The formation of
 349 leaching zones is simulated until the right model boundary is reached by the reaction
 350 front.

351 **3 Results**

352 Figure 7 shows the evolution of the ratio between permeated and total rock volume
 353 (halitic areas not included). In case of low dissolution rates ($k_{max} = 5 \cdot 10^{-6} \text{ cm/s}$), the leaching
 354 zone growth is nearly linear (Figure 7a,b). For all rock distributions, it takes 13-14 years for the
 355 simulations to meet the stop criterion with 96% of the (non-halitic) rock being permeated. Only
 356 in case of the $+10^\circ$ inclination, the growth rate starts to decrease after approximately six years
 357 (Figure 7a) with only 85% of the rock being permeated at the end. Halite inclusions lead to a less

358 regular growth rate compared to the homogeneous case, but strong deviations from linear growth
 359 are not observed (Figure 7b).



360 **Figure 7.** Ratio between permeated and total (soluble) rock volume over time for (a), (c) an
 361 intersecting halite layer and (b), (d) halite inclusions (c.l. = correlation length) compared to the
 362 homogeneous case.

363 In case of high dissolution rates ($k_{max} = 5 \cdot 10^{-4}$ cm/s), the differences between rock
 364 distributions increase (Figure 7c,d). Along a homogeneous potash seam, the leaching zone
 365 expands to the right model boundary in two years showing only a slight decrease in growth rate.
 366 However, only 50% of the rock become permeated, while the other half is not affected. In
 367 contrast, heterogeneous potash seams show permeation ratios of 59-72%, taking up to 3.6 years
 368 until the right model boundary is reached. Intersecting halite layer result in different evolutions
 369 depending on the inclination (Figure 7c). In case of a 0° inclination, the permeation speed is
 370 slightly faster than for the homogeneous case, but the stop criterion is only met when 72% of the
 371 rock are permeated. Therefore, it takes 3.6 years instead of the 2 years in the homogenous case.
 372 In case of a +10° inclination, the leaching zone growth is slower and only 60% of the rock are
 373 permeated within the same time period. An inclination of -10° (Figure 6c) causes the highest
 374 permeation speed with 2.6 years required to reach a 67% permeation or the right model
 375 boundary. Potash seams with halite inclusions show a very similar permeation speed compared
 376 to homogeneous ones (Figure 7d). However, since 66-70% of the (soluble) rock are permeated
 377 (instead of 50%), it takes the reaction front almost twice as long to arrive at the right model

378 boundary. Accordingly, heterogeneities slow down the leaching zone growth in horizontal
379 direction by a factor of 1.25 to 1.8 in case of high dissolution rates.

380 In order to determine if the systems are transport- or reaction-dominated, and if the
381 transport is dominated by advection or diffusion, the dimensionless parameters of Péclet (Pe) and
382 Damköhler (Da) can be used, allowing for a classification into four different cases which show
383 different temporal and spatial evolutions of the leaching zone (Steding et al., 2021). The Péclet
384 number is determined from the flow velocity v , the diffusion coefficient D_f and the characteristic
385 length l following equation (7). Pe has to be calculated individually for each cell, since v varies
386 in space (and time). l is approximated with the current width of the leaching zone, which timely
387 varies in vertical direction.

$$388 \quad Pe = v \cdot l / D_f \quad (7)$$

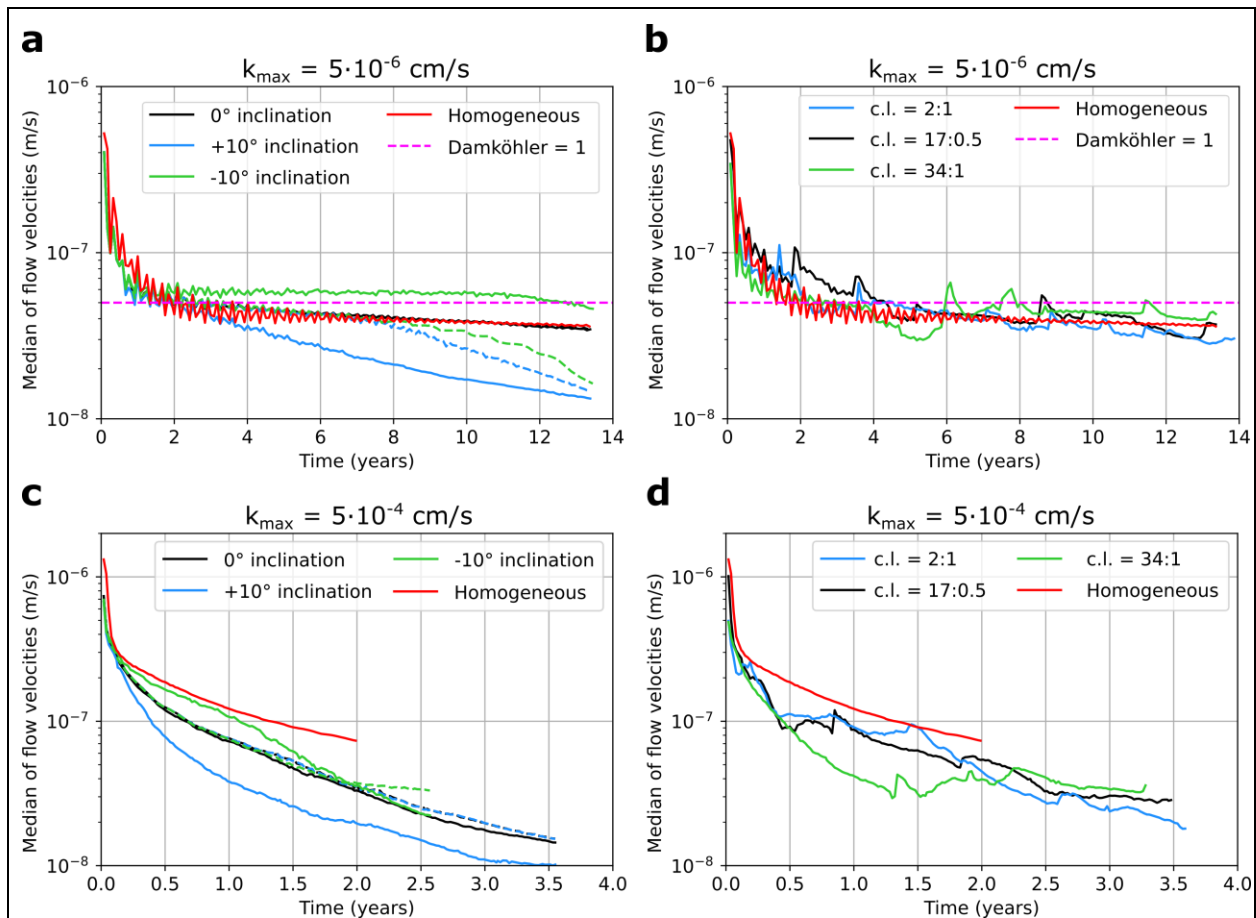
389 To determine if the system is dominated by advection ($Pe > 2$) or diffusion ($Pe < 2$), the
390 median of all permeated cells is determined. All homogeneous and heterogeneous scenarios
391 show a median Péclet number which is clearly above two over the entire modelling period, i.e.
392 all systems are advection-dominated. This means that diffusion is negligible as transport process
393 within the leaching zone and that the Damköhler number, which is defined as the ratio between
394 reaction rate and transport velocity, can be calculated from the flow velocity v according to
395 equation (8). To calculate the reaction rate of each mineral, equation (1) is used considering the
396 saturations of the inflowing solution. The studies of Field et al. (2019) indicate that at the same
397 flow velocity, low saturations cause transport-dominated systems ($Da > 1$), while high
398 saturations result in reaction-dominated systems ($Da < 1$). Since the solution at the left boundary
399 is NaCl-saturated, the reaction rate for halite is zero. In case of sylvite and carnallite, *rate*
400 corresponds to k_{max} since the inflowing solution is highly undersaturated with respect to both
401 minerals. The transport velocity corresponds to the flow velocity calculated by TRANSE.

$$402 \quad Da = \text{reaction rate} / \text{transport velocity} = k_{max} / v \quad (\text{if } Pe > 2) \quad (8)$$

403 A Damköhler number for the system can be derived from k_{max} and the median of all flow
404 velocities within the permeated area. The latter is divided into upper and lower halves in case of
405 intersecting halite layers. Figure 8 shows that the median always ranges between 10^{-6} m/s and 10^{-8}
406 m/s. This means that for $k_{max} = 5 \cdot 10^{-4}$ cm/s, Da is always above one, while for $k_{max} = 5 \cdot 10^{-6}$
407 cm/s, Da falls below one if the flow velocity is above $5 \cdot 10^{-8}$ m/s. In case of homogeneous potash
408 seams, this holds true during the first 2 years of simulation (Figure 8a,b). After that, the decrease
409 in flow velocity results in a Damköhler number slightly above one, eventually equalling 1.4. If
410 the potash seam is intersected by a horizontal halite layer, it takes 3 years to reach $Da = 1$ since
411 the average flow velocity is slightly higher at the beginning (Figure 8a). Later, its decrease is
412 stronger, so that $Da = 1.4$ is eventually reached as well. Similar evolutions can be observed
413 within the upper half of the potash seam if the intersecting halite layer is inclined. However, after
414 7-8 years, the flow velocity decrease becomes faster and Da becomes higher. On the other hand,
415 flow velocities within the lower half are constantly lower for a $+10^\circ$ inclination and constantly
416 higher for a -10° inclination. In the latter case, Da rises above one only after 13 years. In case of
417 halite inclusions, it partly takes more than 2 years to reach $Da = 1$, e.g. for the 17:0.5 distribution,
418 and the evolution of the average flow velocity is less regular resulting in several crossings of Da

419 = 1 over time, e.g. for the 34:1 distribution (Figure 8b). However, the overall evolution of flow
 420 velocities is relatively similar to the homogeneous case.

421

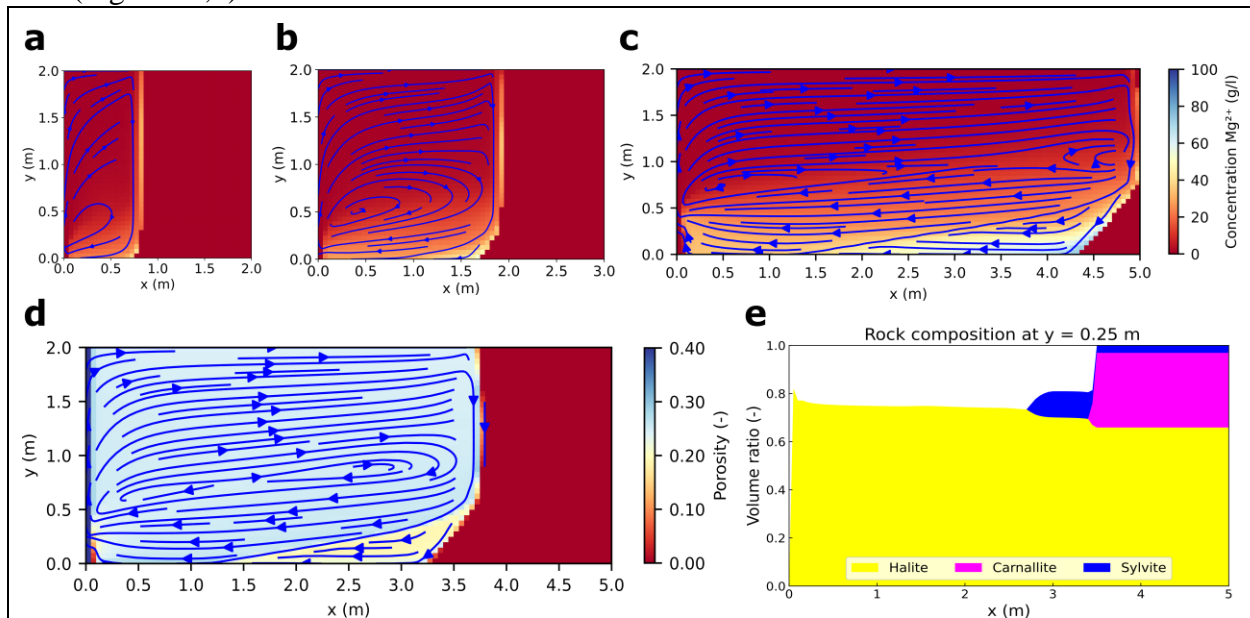


422 **Figure 8.** Median of flow velocities over time for (a), (c) an intersecting halite layer (solid line =
 423 below layer, dotted line = above layer) and (b), (d) halite inclusions (c.l. = correlation length)
 424 compared to the homogeneous case.

425 In contrast, $k_{max} = 5 \cdot 10^{-4}$ cm/s leads to larger deviations in flow velocity (Figure 8c,d).
 426 Thereby, heterogeneous potash seams generally show smaller flow velocities than homogeneous
 427 ones. In case of a horizontal, intersecting layer, both halves show the same decrease in flow
 428 velocity over time and after 2 years, the flow velocity amounts to approximately 50% of that in
 429 the homogeneous case (Figure 8c). The same evolution can be seen within the upper half of
 430 potash seams with intersecting layers at $\pm 10^\circ$ inclination. After 3.6 years, the flow velocities
 431 have decreased to $1.5 \cdot 10^{-8}$ m/s, what represents only 20% of the final flow velocity in the
 432 homogeneous case. However, for a -10° inclination, the velocity decrease is reduced after 2 years
 433 and the right model boundary is reached after 2.6 years already. Within the lower half of the
 434 potash seam, the average flow velocity is smaller compared to the upper half if the inclination of
 435 the intersecting layer is $+10^\circ$. In contrast, it is most of the time higher in case of -10° inclination.
 436 Thus, flow velocities within the lower half show an increased dependency on inclination.
 437 Heterogeneous potash seams with halite inclusions also show a clear trend towards flow velocity
 438 decrease over time (Figure 8d). However, phases of increase occur as well – especially for the

439 34:1 distribution – which cannot be observed for homogeneous potash seams or intersecting
 440 layers.

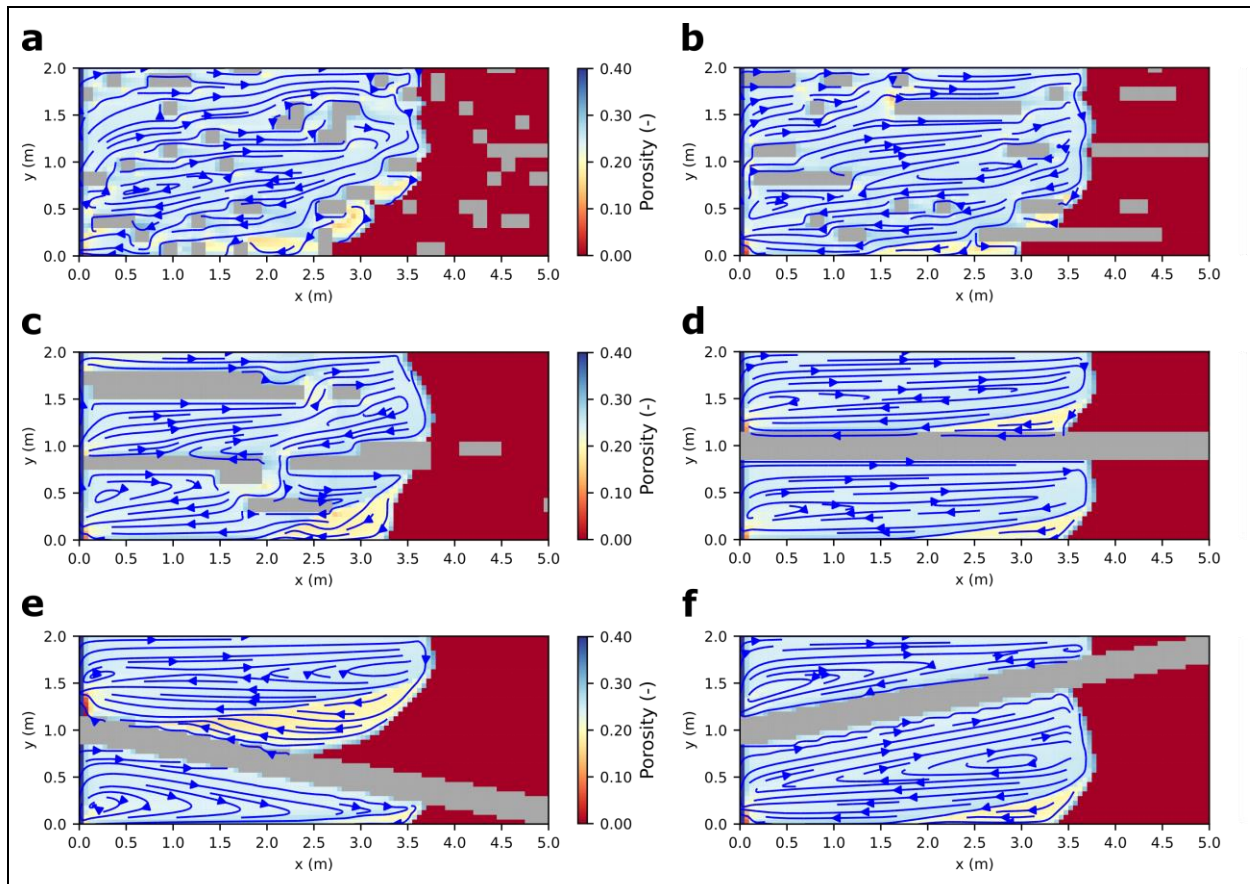
441 To evaluate the shift from reaction- ($Da < 1$) to transport-dominated ($Da > 1$) systems in
 442 case of $k_{max} = 5 \cdot 10^{-6}$ cm/s, the distribution of Mg^{2+} after different time periods is shown in Figure
 443 9. The Mg^{2+} concentration is a useful indicator for fluid density and saturation: absence of Mg^{2+}
 444 usually represents a NaCl solution with a density of $1,200 \text{ kg/m}^3$, while a solution with $>85 \text{ g/l}$
 445 Mg^{2+} (at $25 \text{ }^\circ\text{C}$) has a density of $>1,270 \text{ kg/m}^3$ and is fully saturated with respect to halite, sylvite
 446 and carnallite. In case of homogeneous potash seams (Figure 9), the solution is highly
 447 undersaturated with regard to sylvite and carnallite along the entire dissolution front during the
 448 first two years. Accordingly, both minerals are fully dissolved and only halite remains. In
 449 contrast to halitic areas, the rock is fully permeated and porosity is high ($\approx 30\%$) within these
 450 zones (further referred to as halite zones). The dissolution front is planar during that time, while
 451 concentration and density gradients are comparatively low. However, the Mg^{2+} concentration at
 452 the bottom increases and after 2 years, when $Da=1$ is reached, the dissolution of sylvite and
 453 carnallite is significantly reduced at the lower end of the dissolution front. As a result, a
 454 sylvinitic zone, consisting of halite and sylvite (Figure 9d,e), is formed next to it and an
 455 inclination of the dissolution front occurs. Over time, its upper end moves upwards (Figure 9b,c)
 456 and the sylvinitic zone with lower porosity grows. Additionally, a small barrier is formed next to
 457 the lower end of the inflow due to the precipitation of halite (Figure 9d). Although the average
 458 flow velocity decreases (Figure 8a,b), the growth rate of the leaching zone remains constant over
 459 time (Figure 7a,b).



460 **Figure 9.** Convection cell of a system shifted from a reaction- to a transport-dominated one:
 461 Mg^{2+} concentration distribution after simulation times of (a) two years, (b) five years and (c)
 462 13.4 years; (d) porosity distribution and (e) mineralogical composition after 10 years for a
 463 homogeneous potash seam and $k_{max} = 5 \cdot 10^{-6}$ cm/s.

464 In cases of halite inclusions, the leaching zone evolution is basically similar to the
 465 homogeneous case. However, the more often the dissolution front is disturbed by inclusions, the
 466 more irregular it becomes (Figure 10a-c). The same applies to the sylvinitic zone within the

467 lower area. Apart from that, sylvinitic zones now also occur above or behind inclusions and are
 468 often redissolved as soon as the flow regime changes and local Mg^{2+} concentrations decrease. A
 469 slower growth rate, which is usually associated with a sylvinitic zone next to the dissolution
 470 front, can now be observed within the upper area as well (Figure 10c). Generally, the convection
 471 cell is increasingly divided into smaller sub-cells, the broader inclusions are. However, with
 472 regard to the shape and penetration depth of the leaching zone, differences compared to the
 473 homogeneous case are negligible.

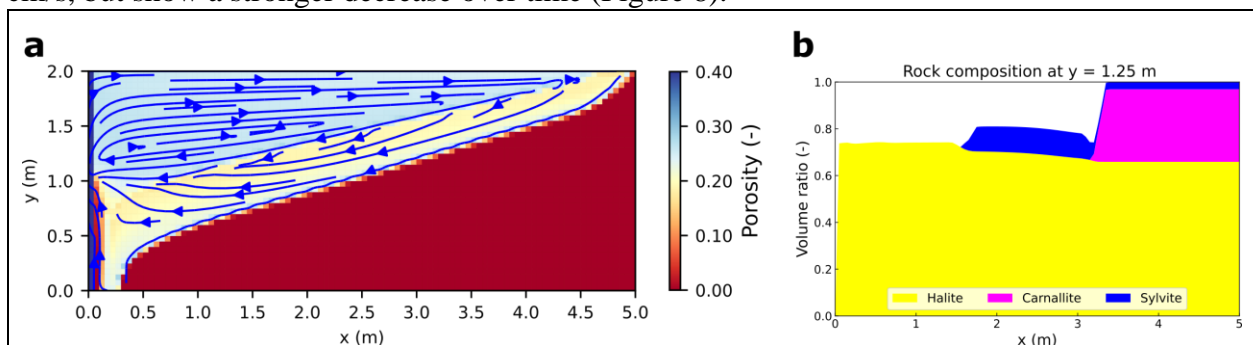


474 **Figure 10.** Porosity distribution after a simulation time of 10 years for heterogeneous potash
 475 seams with halite inclusions for the distributions (a) 2:1, (b) 17:0.5, (c) 34:1 and intersecting
 476 layers with (d) 0° , (e) $+10^\circ$, (f) -10° inclination and $k_{max} = 5 \cdot 10^{-6}$ cm/s.

477 In case of an intersecting, insoluble halite layer, the system is split up into two convection
 478 cells that evolve independently of each other. As shown in Figure 7a, the influence on the growth
 479 rate of the leaching zone is small if the dissolution rate is low ($k_{max} = 5 \cdot 10^{-6}$ cm/s). In case of a
 480 horizontal layer (Figure 10d), both convection cells show nearly the same evolution as that in the
 481 homogeneous case (Figure 9). Although the sylvinitic zone is formed slightly later – after about
 482 3 years instead of 2 years – it quickly covers a larger part of the dissolution front: after 10 years,
 483 approximately 50% of it compared to 30% in the homogeneous case (Figure 9; 10d). However,
 484 the penetration depth at the upper end of the dissolution front is approximately the same. In
 485 contrast, the convection cells develop differently after some years if the intersecting layers are
 486 inclined (Figure 10e-f). Although the upper halves show similar flow velocities as in case of a
 487 horizontal layer during the first 7-8 years (Figure 8a), the sylvinitic zone is formed earlier and

488 grows faster if the height increases (Figure 10e), while it does not occur at all if the height
 489 decreases (Figure 10f). The same applies to the formation of the barrier next to the inflow. On
 490 the other hand, an increasing height within the lower half results in the same sylvinitic zone and
 491 barrier formation as in case of a horizontal layer (Figure 10d,f), although flow velocities are
 492 higher and it takes 13 years to reach $Da=1$ (Figure 8a). If the height within the lower half
 493 decreases, the sylvinitic zone starts forming after about 2.5 years but grows relatively slow. After
 494 10.5 years, it completely covers the dissolution front (Figure 10e), although it is only 1 m wide
 495 and 0.2 m high. From that point in time, the growth rate of the lower half is reduced, while flow
 496 velocities already show a significant decrease after 3 years (Figure 8a). In all other cases, the
 497 maximum penetration depth is the same within the upper and lower layer and the right model
 498 boundary is reached after 13.4 years.

499 For $k_{max} = 5 \cdot 10^{-4}$ cm/s, the Damköhler number is clearly above one during the entire
 500 simulation time and a funnel-shaped leaching zone is formed, showing preferential dissolution
 501 within the upper half of the potash seam (Figure 11). Its width decreases nearly linearly from the
 502 top to the bottom. The lower part of the potash seam is not dissolved, resulting in an increased
 503 flattening of the dissolution front over time. As indicated in Figure 7c-d, the expansion becomes
 504 slower over time: while the leaching zone penetrates 3 m deep into the seam in the first year, it
 505 proceeds only two more metres into the seam within the second year. The precipitation of halite
 506 next to the left model boundary leads to the formation of a flow barrier within the lower half of
 507 the potash seam. Close to the entire dissolution front, a sylvinitic zone is formed (Figure 11a,
 508 yellow). Its maximum width in horizontal direction is reached at the height of the barrier top.
 509 Basically, two different solution compositions exist within the leaching zone. The first one
 510 contains almost no Mg^{2+} and can be found within the halite zone (Figure 11a, blue), while the
 511 second one shows Mg^{2+} concentrations of >70 g/l and is present within the sylvinitic zone
 512 (Figure 11a, yellow). The border reaches from the upper end of the dissolution front to the top of
 513 the barrier and represents an area with large concentration gradients. Thus, there is a large
 514 density gradient at the border as well, representing the driving force of the free convection.
 515 Figure 11a shows that above this border, fluid flow proceeds mainly from left to right, while
 516 below it the (highly saturated) solution is moving from the dissolution front back towards the left
 517 boundary. The resulting flow velocities are higher at the beginning compared to $k_{max} = 5 \cdot 10^{-6}$
 518 cm/s, but show a stronger decrease over time (Figure 8).

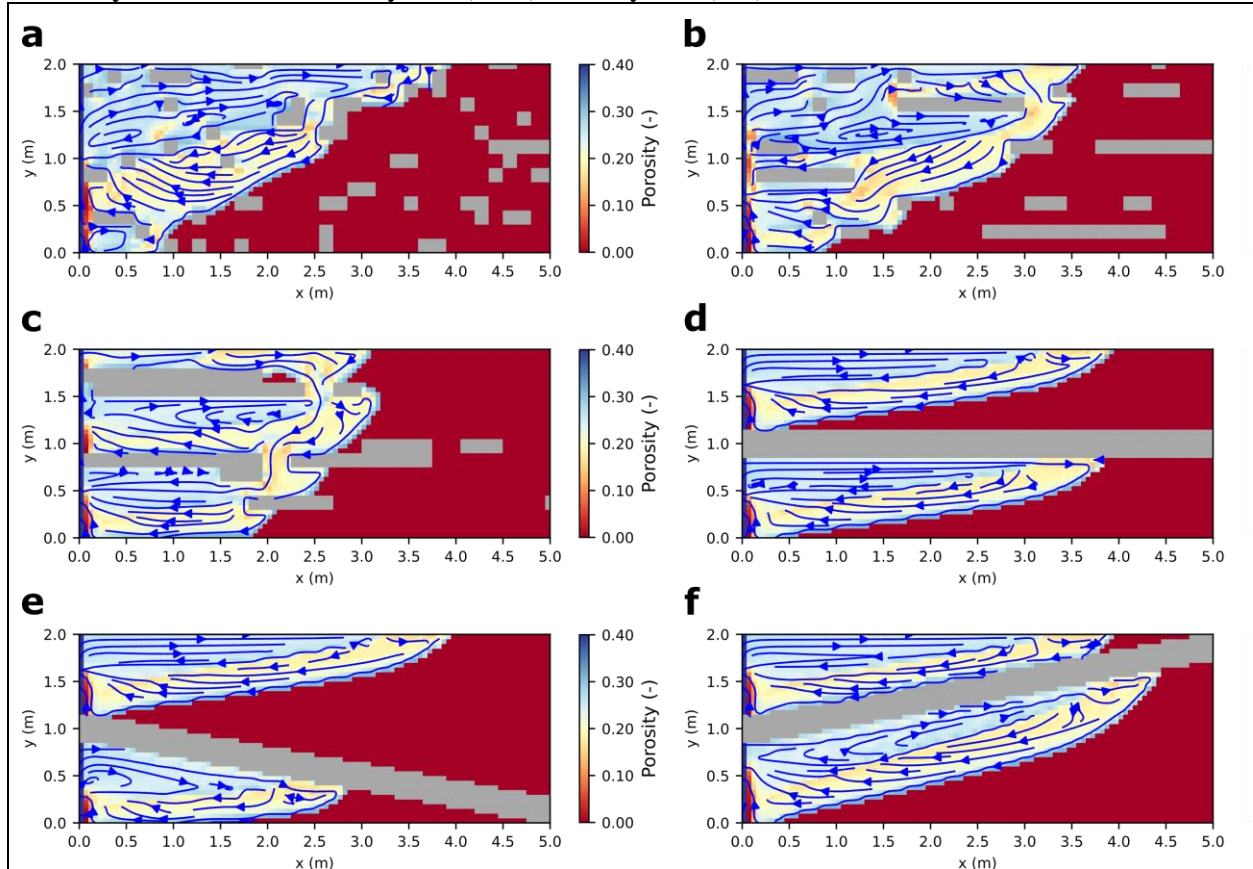


519 **Figure 11.** Convection cell of a fully transport-dominated system: (a) Porosity distribution and
 520 (b) mineralogical composition after a simulation time of 2 years for a homogeneous potash seam
 521 and $k_{max} = 5 \cdot 10^{-4}$ cm/s

522 In case of $k_{max} = 5 \cdot 10^{-4}$ cm/s, halite inclusions lead to smaller, less regular flow velocities
 523 in space and time (Figure 8d). In case of small and medium-sized inclusions, the flow field still

524 shows one main convection cell with undersaturated inflowing solution, mainly present within
525 the upper-left area of the leaching zone, and highly saturated outflowing solution along the
526 dissolution front and within the lower area (Figure 12a,b). Accordingly, the shape of sylvinitic
527 zone and barrier remains basically similar to the homogeneous case. However, zones containing
528 only halite now also occur within the lower half of the leaching zone behind the barrier. In
529 return, wide sylvinitic zones can occur in the upper half especially above inclusions (Figure 12b).
530 Neither the inclination of the dissolution front nor of the border between the halite and sylvinitic
531 zone is linear any more and the lower end of the dissolution front is about 1 m away from the
532 inflow compared to 0.25 m in the homogeneous case (Figure 11a; 12a,b). In case of broader
533 inclusions, the flow field shows three smaller convection cells after 10 years with each having its
534 own barrier at the left (Figure 12c). The same applies to the sylvinitic zone. The dissolution front
535 is subdivided into 3-4 sections with different penetration depths. Thereby, the upper one shows
536 lower dissolution rates than the one below, leading to a recess at 1.6 m height. However, this
537 phenomenon quickly disappears as soon as the upper half of the dissolution front is not
538 subdivided any more and the flow regime changes accordingly. Between large inclusions, the
539 flow is not disturbed and the dissolution front as well as the borders between halite and sylvinitic
540 zones are nearly as regular as in the homogeneous case (Figure 11a). However, the overall
541 inclination of the dissolution front is much steeper. As a result, the same permeation speed leads
542 to smaller penetration depths within the upper part of the potash seam after 2 years, but higher

543 permeation ratios at the end for all cases of halite inclusions (Figure 7d). Here, the right model
 544 boundary is reached after 3.3 years (34:1) to 3.6 years (2:1).



545 **Figure 12.** Porosity distribution after a simulation time of 2 years for heterogeneous potash
 546 seams with halitic inclusions for distributions of (a) 2:1, (b) 17:0.5, (c) 34:1 and intersecting
 547 layers with (d) 0° , (e) $+10^\circ$, (f) -10° inclination and $k_{max} = 5 \cdot 10^{-4}$ cm/s.

548 The leaching zones above intersecting layers show nearly similar evolutions in
 549 penetration depth regardless of the inclination (Figure 12d-f). If the height is constant or
 550 increases, shape and flow velocities evolve similarly as well (Figure 12d,e; 8d), while in case of
 551 decreasing height, the dissolution front follows the intersecting layer (Figure 12f) and the
 552 penetration speed slightly decreases as the height falls below 0.25 m. Compared to the
 553 homogeneous case, the width of the leaching zone shows a lower decrease within the upper half
 554 and a higher one within the lower half, resulting in higher permeation ratios (Figure 7c). Only if
 555 the height increases, a large area of undissolved potash salt is maintained between the
 556 intersecting layer and the upper leaching zone, leading to an overall permeation ratio of 59%
 557 (compared to $>70\%$ for 0° and -10° inclination) at the end of the simulation time (Figure 7c;
 558 12e). After 2 years, the barrier covers about half of the upper in- and outflow region and the right
 559 model boundary is reached after 3.5 years. However, in case of a -10° inclination, the lower
 560 leaching zone grows faster than the upper one (Figure 12f). Thus, the right model boundary is
 561 already reached after 2.6 years. In contrast, the $+10^\circ$ inclination results in smaller growth rates
 562 within the lower half (Figure 12e). Generally, layers with increasing height grow faster, while
 563 layers with decreasing height show higher permeation ratios (Figure 12e,f). Compared to the

564 homogeneous case, sylvinitic zones (yellow) are slightly broader at the upper end of the
565 dissolution front in all cases of intersecting layers.

566 **4 Discussion**

567 The results show that the influence of insoluble inclusions and intersecting layers
568 strongly depends on the dissolution rate of the soluble minerals. In case of low dissolution rates
569 ($k_{max} = 5 \cdot 10^{-6}$ cm/s), the evolution of the leaching zone is only slightly affected (Figure 7a,b; 10),
570 although local and average flow velocities are significantly changed (Figure 8a,b). In contrast,
571 heterogeneities lead to a reduction in penetration depth (Figure 12) and higher permeation ratios
572 (Figure 7c,d) if dissolution rates are high ($k_{max} = 5 \cdot 10^{-4}$ cm/s). These differences can be explained
573 by a distinction between reaction-dominated and transport-dominated systems. A fully reaction-
574 dominated system ($Da \ll 1$) is given if the effective dissolution rates of sylvite and carnallite
575 according to equation (1) correspond to the maximum dissolution rate, i.e. if their saturation only
576 shows a very slight increase along the dissolution front. In this case, the dissolution front is
577 planar and neither local nor overall changes in flow velocity affect the growth rate of the
578 leaching zone: it is entirely controlled by the reaction speed. This case is given for $k_{max} = 5 \cdot 10^{-6}$
579 cm/s at the start of the simulation. However, after some years, the saturations along the
580 dissolution front become high enough to significantly reduce the dissolution rate of sylvite and
581 carnallite, making the system only partly reaction-dominated ($Da \approx 1$). The reason for that can be
582 a decrease in flow velocity or an increase in the length of the dissolution front. As a result, the
583 dissolution front becomes inclined and a sylvinitic zone as well as a barrier are formed (Figure
584 9). If the entire dissolution front is inclined and covered by a sylvinitic zone, the system is fully
585 transport-dominated ($Da \gg 1$) as given for $k_{max} = 5 \cdot 10^{-4}$ cm/s. These systems are much more
586 sensitive to changes in flow velocity. Therefore, they are much more affected by heterogeneities
587 influencing both, the local distribution and the average flow velocity (Figure 8; 10; 12).

588 The Damköhler number is a useful indicator to determine if a system is dominated by
589 reaction or transport (Weisbrod et al., 2012; Oltéan et al., 2013; Steding et al., 2021). Generally,
590 the simulation results show that an overall Da calculated from the average flow velocity and the
591 saturation-dependent dissolution rate of the inflowing solution corresponds to the observed
592 leaching zone shapes. In case of $k_{max} = 5 \cdot 10^{-4}$ cm/s, $Da \gg 1$ is given and a funnel-shape can be
593 observed including a barrier at the left and a sylvinitic zone along the entire dissolution front
594 (Figure 11). These are typical indicators for a transport-dominated system (Steding et al., 2021).
595 In case of $k_{max} = 5 \cdot 10^{-6}$ cm/s, the dissolution front is planar in the beginning when $Da < 1$, while
596 it becomes inclined as Da rises above one with a sylvinitic zone and barrier rising from the
597 bottom (Figure 8a,b; 9a-c). However, insoluble inclusions make it more difficult to identify this
598 point in time, because the average flow velocity evolves less regularly (Figure 8b) and strong
599 local deviations occur, resulting in small sylvinitic zones near the inclusions and a more irregular
600 dissolution front (Figure 10a-c). In case of intersecting layers, Da has to be determined for each
601 sub-system or convection cell, and if the layer is inclined, the time period in which Da rises
602 above one does no longer correlate with the formation of sylvinitic zones and barriers (Figure 8a;
603 10d-f). From our point of view, the reason for this is a change in the length of the dissolution
604 front: if it increases, higher saturations can be reached at the bottom without a change in flow
605 velocity and vice versa. All in all, the larger the heterogeneities are, the less appropriate an
606 overall Damköhler number is to determine if the system is dominated by reactions or transport.
607 Additionally, it has to be noted that complex systems containing several minerals can be
608 reaction- and transport-dominated at once: if the maximum dissolution rate k_{max} or the saturations

609 of the inflowing solution vary a lot for different minerals, some of them will show $Da > 1$, while
610 others show $Da < 1$. Accordingly, the Damköhler number has to be calculated individually for
611 each mineral and an internal contact area between equilibrated and non-equilibrated minerals has
612 to be defined (Figure 4) to reproduce the formation of several dissolution fronts as those
613 observed by Ahoulou et al. (2020). In this case, heterogeneities are expected to mainly influence
614 the dissolution pattern of minerals with $Da > 1$.

615 Heterogeneities also affect the hazard potential of leaching zones by influencing the
616 growth rate, shape and permeation ratio. In this context, higher growth rates are associated with
617 faster expansion of the leaching zone and an increasing risk of mine flooding or integrity loss of
618 a cavern. Higher permeation ratios or porosities also increase the hazard potential as they result
619 in a lower mechanical stability as well as larger solution amounts stored per metre leaching zone.
620 The results show that for $Da \gg 1$, insoluble inclusions mainly affect the shape: at the top, the
621 dissolution front is progressing relatively slow, whereas at the bottom dissolution rates are higher
622 compared to the homogeneous case (Figure 11; 12a-c). As a result, the permeation speed is
623 basically the same (Figure 7d), but the dissolution front is steeper and it takes 1.65-1.8 times
624 longer until the right model boundary is reached. It is important to note that the distribution of
625 insoluble inclusions does not have a significant influence if their volume ratio is identical.
626 Although broader inclusions increasingly split up the convection cell into smaller ones and lead
627 to a more irregular average flow velocity, the overall evolution is always quite similar (Figure
628 7d; 8d; 12a-c). Thereby, the leaching zone growth in horizontal direction is slower compared to
629 the homogeneous case, but the permeation ratio is higher at the end of the simulation, what can
630 become more critical with regard to mechanical stability. In case of one continuous insoluble
631 layer, the leaching zone consists of two independent convection cells, showing the same regular
632 dissolution front, sylvinitic zone and barrier as in the homogeneous case. However, flow
633 velocities and permeation speed are more similar to those of insoluble inclusions (Figure 7c; 8c;
634 12d). Inclined, intersecting layers particularly influence the flow velocity within the lower half
635 (Figure 8c). Thereby, negative inclinations increase the flow velocity resulting in faster leaching
636 zone growth compared to the upper half (Figure 12f) and vice versa. The evolution of the upper
637 half is basically not influenced (Figure 12e,f). However, the amount of undissolved potash rock
638 is larger with increasing height, resulting in relatively small permeation ratios (Figure 7c). In
639 summary, an intersecting layer with negative inclination is the most critical distribution of
640 insoluble inclusions, leading to higher permeation ratios and only slightly smaller growth rates in
641 horizontal direction compared to the homogeneous case.

642 Field observations indicate that the formation of caverns and leaching zones in salt rock
643 is usually dominated by transport. According to Koch and Vogel (1980), the upper half of a
644 potash seam is often preferentially dissolved and natural leaching zones within carnallitic rock
645 are mostly divided into a halite zone near the inflow region and a sylvinitic zone close to the
646 dissolution front. These observations agree with the results for a transport-dominated system
647 ($k_{max} = 5 \cdot 10^{-4}$ cm/s) of homogeneous rock composition (Figures 11). In case of intersecting layers
648 from pure halite, Koch and Vogel (1980) assume a split into several dissolution fronts with
649 different penetration depths. A similar phenomenon has been observed in solution mining: if
650 several insoluble layers cross the salt body, the resulting cavern shape resembles an inverted
651 Christmas tree (Thoms & Gehle, 1999). The same shape is described by Fokker (1995) for
652 technical caverns crossing different (potash) salt layers. Furthermore, Fokker (1995) implies that
653 inclined layers cause an asymmetric shape, whereby the growth rate is faster in the direction of

654 upward-directed inclination. These descriptions all correspond to the simulation results for a
655 transport-dominated system with intersecting halite layers (Figures 12d-f). However, time frames
656 for the evolution of natural leaching zones are not available. Regarding insoluble inclusions,
657 laboratory experiments conducted by Gechter et al. (2008) and Field et al. (2019) confirm that
658 the cavern shape becomes increasingly distorted and notches occur at the dissolution front if
659 insoluble lenses impede regular fluid flow (Figures 12a-c). Also consistent is the finding that
660 inclusions do not reduce the amount of dissolved/permeated rock per time but only its
661 distribution (Figures 7d) (Gechter et al., 2008). Reaction-dominated systems with (nearly) planar
662 dissolution fronts only occur if the inflowing solution is already highly saturated with respect to
663 the present salt minerals (Field et al., 2019). In this case, significantly slower growth rates as
664 well as an increased influence of rock fabric were observed. The first finding agrees with our
665 simulation results (Figures 7), while the second one could not be reproduced (Figures 10a-c). All
666 in all, there is a good correlation between literature data and model results regarding the
667 influence of heterogeneities. However, the temporal scaling is still uncertain and more data are
668 required for a comprehensive quantitative model validation.

669 Finally, the results reveal how saturation-dependent dissolution rates affect barrier
670 formation and leaching zone shape. In case of fully reaction-dominated systems ($Da \ll 1$), there
671 is no difference compared to constant dissolution rates because k_{max} is always reached. In
672 contrast, transport-dominated systems show a more linear decrease in width from the top to the
673 bottom, since the effective dissolution rate decreases along the dissolution front. Therefore, a
674 longer distance is required until the solution is fully saturated and the transition from dissolved to
675 undissolved sections of the potash seam is less sharp compared to constant dissolution rates
676 (Steding et al., 2021). Additionally, the barrier next to the inflow is smaller, resulting in a less
677 decreasing flow velocity and growth rate over time. Thus, saturation-dependent dissolution rates
678 lead to a wider extension and therefore a higher hazard potential of the leaching zone in the long
679 term. Furthermore, they intensify the coupling between chemical reactions and transport. Next to
680 the dissolution front, where strong concentration gradients occur, changes in advection,
681 diffusion or dispersion immediately affect the saturations, and therefore the effective dissolution
682 rates. In return, the dissolved mineral amounts affect transport parameters such as brine density,
683 viscosity and diffusion coefficients. An even stronger coupling would be achieved if k_{max} is
684 treated as a function of flow velocities. Several studies indicate that for fast dissolving minerals,
685 such as most potash salts, the dissolution rate is controlled by the transport across a so-called
686 diffusive boundary layer that is formed at the mineral-fluid interface (Alkattan et al., 1997; De
687 Baere et al., 2016; Dutka et al., 2020). Thereby, higher fluid flow velocities induce a decrease in
688 thickness of the boundary layer, and therefore higher dissolution rates of the minerals. As a
689 result, k_{max} varies locally and heterogeneities may have a stronger effect. However, the approach
690 uses input parameters, such as the reaction rate constant, which are currently not known for
691 many potash minerals. Furthermore, knowledge about the flow field at pore scale and the bulk
692 concentrations outside the boundary layer are required (Molins et al., 2012). Both are hard to
693 determine by continuum-scale models which cannot exactly reproduce the concentration
694 distribution at the dissolution front. By using average saturations to calculate the dissolution
695 rates, an artificial mixing is always generated, influencing the leaching zone shape or the fluid
696 flow path until full saturation is reached. Accordingly, a calibration of the model based on
697 experimental data is crucial. All in all, the simulation results show that the saturation-
698 dependency of dissolution rates has a significant influence on the leaching zone evolution in case

699 of partly or fully transport-dominated systems ($Da \geq 1$), and therefore needs to be considered
700 when investigating further scenarios.

701 **5 Conclusions and outlook**

702 The reactive transport model presented here takes into account the local saturation state
703 of each mineral for the calculation of its dissolution rate. As a result, highly undersaturated
704 minerals are dissolved relatively fast, while others remain undissolved. In case of the carnallite-
705 bearing potash seam used for our scenario analysis, areas from pure halite are insoluble because
706 the inflowing solution is constantly NaCl-saturated. The results show that insoluble inclusions
707 and intersecting layers mainly influence the evolution of advection- and transport-dominated
708 systems ($Pe > 2$ and $Da > 1$). Thereby, the amount of potash salt permeated over time is similar
709 to the homogeneous case, whereas the shape of the leaching zone is different. Although the
710 upper half of the potash seam is still preferentially dissolved, the dissolution front becomes
711 steeper in case of insoluble inclusions. In case of intersecting layers, two independent leaching
712 zones evolve. All cases have in common that the upper end of the dissolution front(s) moves
713 forward 1.8 times slower and, in return, the permeation ratio of the potash seam increases from
714 50% to 59-72% at the end of the simulation time. Interestingly, the distribution of the insoluble
715 areas is of minor importance: only if these appear as an intersecting layer with negative
716 inclination, the growth rate is 1.25 times lower instead of 1.8. Generally, inclined layers result in
717 an asymmetric expansion of the leaching zone with the upward-directed inclination showing
718 faster growth rates. In case of advection- and reaction-dominated systems ($Pe > 2$ and $Da < 1$),
719 the influence of heterogeneities on the leaching zone evolution is negligible. Although the
720 dissolution front becomes less regular, the growth rate, shape and porosity of the leaching zone
721 remain basically unaffected. Literature data indicate that most systems in nature are transport-
722 dominated.

723 With regard to risk assessment, insoluble areas within potash seams can usually be seen
724 as beneficial. At best, they slow down leaching zone growth, while at worst they do not. In order
725 to assess their influence, the Damköhler number is a useful indicator that can be determined from
726 the average flow velocity and the effective dissolution rate(s) of the inflowing solution.
727 However, Da has to be calculated individually for each mineral and, in case of intersecting
728 layers, also for each separate leaching zone. Heterogeneities influence the local and average flow
729 velocities and can shift the transition time from a reaction- to a transport-dominated system.
730 Especially inclined intersecting layers reduce the validity of the Da indicator. However, the
731 occurrence of funnel-shapes, barriers and sylvinitic zones (in case of carnallitic potash salt), can
732 be seen as a clear evidence for transport-dominated systems ($Da > 1$). In contrast, planar
733 dissolution fronts and an effluent solution that is not fully saturated with regard to the present
734 minerals indicate a reaction-dominated system ($Da < 1$). The first kind of systems evolves
735 generally faster in the beginning, but the growth rate is reduced by barrier formation and
736 heterogeneities (if present). However, it has to be noted that with regard to the solution amount
737 and mechanical stability, heterogeneities may increase the hazard potential due to the higher
738 permeation ratios of 59-72%. Reaction-dominated systems show a slow but steady growth that is
739 not reduced by heterogeneities. The potash seam becomes fully permeated and all minerals
740 undersaturated with regard to the inflowing solution are dissolved. Thus, the collapse of
741 insoluble layers and/or large inclusions as described by Anderson and Kirkland (1980) or Warren

742 (2017) has to be considered if the mechanical stability of the remaining rock matrix is
743 insufficient.

744 The extension of the reactive transport model by variable saturation-dependent
745 dissolution rates has improved its accuracy with regard to leaching zone shape, growth rate and
746 barrier formation. It is shown that constant dissolution rates overestimate the barrier formation,
747 and therefore underestimate the hazard potential in the long-term. In the next step, it is planned
748 to not only distinguish between insoluble and highly soluble minerals but to also include slower
749 dissolving minerals such as anhydrite (CaSO_4) or kieserite ($\text{MgSO}_4 \cdot \text{H}_2\text{O}$) into the model by
750 using individual maximum dissolution rates. In doing so, the effects of mineral heterogeneity
751 (Liu et al., 2017) can be investigated in further detail. However, for many secondary minerals
752 occurring in these complex quinary or hexary systems (Steding et al., 2020), k_{max} is not known.
753 Furthermore, a dependency on the local flow velocity is expected to intensify the coupling
754 between chemical reactions and transport. Therefore, laboratory and field measurement data are
755 required to calibrate k_{max} and, on this basis, to model the evolution of leaching zones within
756 potash seams of any composition in space and time.

757 **Acknowledgments**

758 The authors like to thank the German Federal Ministry of Education and Research for the
759 financial support of the project. Furthermore, we thank Axel Zirkler and Dr. Thomas Radtke
760 from K+S for many informative discussions and useful pieces of advice regarding the model
761 conceptualization.

762 **Availability Statements**

763 Datasets have not been used for this publication.

764 The software GSTools and PHREEQC are available in these in-text data citation
765 references: Müller & Schüler (2021), Parkhurst & Appelo (2013)

766 The software TRANSE is described in Kempka (2020) with the code being currently in
767 publication process.

768 The coupling of PHREEQC and TRANSE was done in Python 3 which is available in
769 this in-text data citation reference: Van Rossum & Drake (2009).

770 The model output data and the Jupyter notebook to execute the analysis in the paper will
771 be published via GFZ Data Services (<https://dataservices.gfz-potsdam.de/portal/about.html>) and
772 are currently (for an exemplary scenario) available at Nextcloud via [https://nextcloud.gfz-](https://nextcloud.gfz-potsdam.de/s/QcQmgf5QAqzwoTQ)
773 [potsdam.de/s/QcQmgf5QAqzwoTQ](https://nextcloud.gfz-potsdam.de/s/QcQmgf5QAqzwoTQ).

774 **References**

- 775 Ahoulou, A.W.A., Tinet, A.J., Oltéan, C. & Golfier, F. (2020), Experimental Insights Into the
776 Interplay Between Buoyancy, Convection, and Dissolution Reaction. *Journal of*
777 *Geophysical Research: Solid Earth*, 125(11), 1–18. doi:10.1029/2020JB020854
- 778 Alkattan, M., Oelkers, E., Dandurand, J. & Schott, J. (1997), Experimental studies of halite
779 dissolution kinetics, 1 The effect of saturation state and the presence of trace metals.
780 *Chemical Geology*, 137(3–4), 201–219. doi:10.1016/S0009-2541(96)00164-7

- 781 Altmaier, M., Brendler, V., Bube, C., Neck, V., Marquardt, C., Moog, H.C., Richter, A.,
782 Scharge, T., et al. (2011), *THEREDA - Thermodynamische Referenz-Datenbasis* (Rep.
783 265). Braunschweig, Germany: Gesellschaft für Anlagen- und Reaktorsicherheit (GRS).
784 Retrieved from <https://www.thereda.de/en/>
- 785 Anderson, R.Y. & Kirkland, D.W. (1980), Dissolution of salt deposits by brine density flow.
786 *Geology*, 8(2), 66–69. doi:10.1130/0091-7613(1980)8<66:DOSDBB>2.0.CO;2
- 787 Boys, C. (1993), A Geological Approach to Potash Mining Problems in Saskatchewan, Canada.
788 *Exploration and Mining Geology*, 2(2), 129–138.
- 789 De Baere, B., Molins, S., Mayer, K.U. & François, R. (2016), Determination of mineral
790 dissolution regimes using flow-through time-resolved analysis (FT-TRA) and numerical
791 simulation. *Chemical Geology*, 430(2016), 1–12. doi:10.1016/j.chemgeo.2016.03.014
- 792 Dijk, P.E. & Berkowitz, B. (2000), Buoyancy-driven dissolution enhancement in rock fractures.
793 *Geology*, 28(11), 1051–1054. doi:10.1130/0091-7613(2000)28<1051:BDEIRF>2.0.CO;2
- 794 Dreybrodt, W. & Buhmann, D. (1991), A mass transfer model for dissolution and precipitation
795 of calcite from solutions in turbulent motion. *Chemical Geology*, 90(1–2), 107–122.
796 doi:10.1016/0009-2541(91)90037-R
- 797 Durie, R.W. & Jessen, F.W. (1964), Mechanism of the Dissolution of Salt in the Formation of
798 Underground Salt Cavities. *Society of Petroleum Engineers Journal*, 4(02), 183–190.
799 doi:10.2118/678-pa
- 800 Dutka, F., Starchenko, V., Osselin, F., Magni, S., Szymczak, P. & Ladd, A. J.C. (2020), Time-
801 dependent shapes of a dissolving mineral grain: Comparisons of simulations with
802 microfluidic experiments. *Chemical Geology*, 540(2019), 119459.
803 doi:10.1016/j.chemgeo.2019.119459
- 804 Field, L.P., Milodowski, A.E., Evans, D., Palumbo-Roe, B., Hall, M.R., Marriott, A.L., Barlow,
805 T. & Devez, A. (2019), Determining constraints imposed by salt fabrics on the
806 morphology of solution-mined energy storage cavities, through dissolution experiments
807 using brine and seawater in halite. *Quarterly Journal of Engineering Geology and*
808 *Hydrogeology*, 52(2), 240–254. doi:10.1144/qjgeh2018-072
- 809 Fokker, P.A. (1995) *The behaviour of salt and salt caverns* (Doctoral dissertation). Retrieved
810 from: <http://repository.tudelft.nl/view/ir/uuid:6847f8e4-3b09-4787-be02-bcce9f0eed06/>.
- 811 Gechter, D., Huggenberger, P., Ackerer, P. & Niklaus Waber, H. (2008), Genesis and shape of
812 natural solution cavities within salt deposits. *Water Resources Research*, 44(11), 1–18.
813 doi:10.1029/2007WR006753
- 814 Höntzsch, S. & Zeibig, S. (2014). *Geogenic caverns in rock salt formations - a key to the*
815 *understanding of genetic processes and the awareness of hazard potential* Poster
816 presented at GeoFrankfurt 2014, Frankfurt a.M., Germany.
- 817 Hoppe, H. & Winkler, F. (1974), Beitrag zur Lösekinetik von Mineralien der Kaliindustrie.
818 *Wissenschaftliche Zeitschrift Techn. Hochsch. Chem. Leuna-Merseburg*, 16(1), 23–28.
- 819 Jinlong, L., Wenjie, X., Jiangjing, Z., Wei, L., Xilin, S. & Chunhe, Y. (2020), Modeling the
820 mining of energy storage salt caverns using a structural dynamic mesh. *Energy*, 193,
821 116730. doi:10.1016/j.energy.2019.116730

- 822 Keime, M., Charnavel, Y., Lampe, G. & Theylich, H. (2012). *Obstruction in a salt cavern :
823 Solution is dissolution* Paper presented at World Gas Conference 2012, Kuala Lumpur,
824 Malaysia.
- 825 Kempka, T. (2020), Verification of a Python-based TRANsport Simulation Environment for
826 density-driven fluid flow and coupled transport of heat and chemical species. *Advances in
827 Geosciences*, 54, 67-77. doi:10.5194/adgeo-54-67-2020
- 828 Koch, K. & Vogel, J. (1980). Zu den Beziehungen von Tektonik, Sylvinitbildung und
829 Basaltintrusionen im Werra-Kaligebiet (DDR). *Freiberger Forschungshefte*.(C 347).
830 Leipzig: VEB Deutscher Verlag für Grundstoffindustrie.
- 831 Li, J., Shi, X., Yang, C., Li, Y., Wang, T. & Ma, H. (2018), Mathematical model of salt cavern
832 leaching for gas storage in high-insoluble salt formations. *Scientific Reports*, 8(1), 372.
833 doi:10.1038/s41598-017-18546-w
- 834 Liu, M., Shabaninejad, M. & Mostaghimi, P. (2017), Impact of mineralogical heterogeneity on
835 reactive transport modelling. *Computers and Geosciences*, 104, 12–19.
836 doi:10.1016/j.cageo.2017.03.020
- 837 Mengel, K., Röhlig, K.J. & Geckeis, H. (2012), Endlagerung radioaktiver Abfälle. *Chemie in
838 Unserer Zeit*, 46(4), 208–217. doi:10.1002/ciuz.201200582
- 839 Molins, S., Trebotich, D., Steefel, C.I. & Shen, C. (2012), An investigation of the effect of pore
840 scale flow on average geochemical reaction rates using direct numerical simulation.
841 *Water Resources Research*, 48(3), 1–11. doi:10.1029/2011WR011404
- 842 Müller, S. & Schüler, L. GeoStat-Framework/GSTools. *Zenodo*. doi:10.5281/zenodo.1313628
- 843 Oltéan, C., Golfier, F. & Buès, M.A. (2013), Numerical and experimental investigation of
844 buoyancy-driven dissolution in vertical fracture. *Journal of Geophysical Research: Solid
845 Earth*, 118(5), 2038–2048. doi:10.1002/jgrb.50188
- 846 Palandri, J.L. & Kharaka, Y.K. (2004), *A compilation of rate parameters of water-mineral
847 interaction kinetics for application to geochemical modeling* (Rep. 2004/1068). Menlo
848 Park, CA: U.S. Geological Survey (USGS). Retrieved from: [http://www.dtic.mil/cgi-
849 bin/GetTRDoc?Location=U2&doc=GetTRDoc.pdf&AD=ADA440035](http://www.dtic.mil/cgi-bin/GetTRDoc?Location=U2&doc=GetTRDoc.pdf&AD=ADA440035)
- 850 Parkhurst, D.L. & Appelo, C.A.J. (2013). Description of Input and Examples for PHREEQC
851 Version 3 - a Computer Program for Speciation, Batch-reaction, One-dimensional
852 Transport, and Inverse Geochemical Calculations. In *Techniques and Methods* (book 6,
853 chapter A43, 497 p.). Denver, CO: U.S. Geological Survey (USGS). doi:10.3133/tm6A43
- 854 Prugger, F.F. & Prugger, A.F. (1991), Water problems in Saskatchewan potash mining - what
855 can be learned from them?. *Underground Mining*, 84(945), 58–66.
- 856 Raines, M.A. & Dewers, T.A. (1997), Mixed transport/reaction control of gypsum dissolution
857 kinetics in aqueous solutions and initiation of gypsum karst. *Chemical Geology*, 140(1–
858 2), 29–48. doi:10.1016/S0009-2541(97)00018-1
- 859 Röhr, H.U. (1981), Lösungsgeschwindigkeiten von Salzmineralen beim Ausspülen von
860 Hohlräumen im Salz. *Kali und Steinsalz*, 8(4), 103–111.

- 861 Steding, S., Kempka, T., Zirkler, A. & Kühn, M. (2021), Spatial and temporal evolution of
862 leaching zones within potash seams reproduced by reactive transport simulations. *Water*,
863 *13*(2). doi:10.3390/w13020168
- 864 Steding, S., Zirkler, A. & Kühn, M. (2020), Geochemical reaction models quantify the
865 composition of transition zones between brine occurrence and unaffected salt rock.
866 *Chemical Geology*, *532*, 119349. doi:10.1016/j.chemgeo.2019.119349
- 867 Thoms, R.L. & Gehle, R.M. (1999), Non-halites and fluids in salt formations, and effects on
868 cavern storage operations. *Geotechnical Special Publication*, *90*, 780–796.
- 869 Warren, J.K. (2017), Salt usually seals, but sometimes leaks: Implications for mine and cavern
870 stabilities in the short and long term. *Earth-Science Reviews*, *165*, 302–341.
871 doi:10.1016/j.earscirev.2016.11.008
- 872 Van Rossum, G., & Drake, F.L. (2009), *Python 3 Reference Manual* (Version 3.7.9). Scotts
873 Valley, CA: CreateSpace. Retrieved from: <https://www.python.org/downloads/>
- 874 Wei, W., Varavei, A., Sanaei, A. & Sepehrnoori, K. (2019), Geochemical Modeling of
875 Wormhole Propagation in Carbonate Acidizing Considering Mineralogy Heterogeneity.
876 *SPE Journal*, *24*(05), 2163–2181. doi:10.2118/195593-pa
- 877 Weisbrod, N., Alon-Mordish, C., Konen, E. & Yechieli, Y. (2012), Dynamic dissolution of
878 halite rock during flow of diluted saline solutions. *Geophysical Research Letters*, *39*(9),
879 L09404. doi:10.1029/2012GL051306
- 880 Xie, M., Kolditz, O. & Moog, H.C. (2011), A geochemical transport model for thermo-hydro-
881 chemical (THC) coupled processes with saline water. *Water Resources Research*, *47*(2),
882 W02545. doi:10.1029/2010WR009270
- 883 Yang, X., Liu, X., Zang, W., Lin, Z. & Wang, Q. (2017), A Study of Analytical Solution for the
884 Special Dissolution Rate Model of Rock Salt. *Advances in Materials Science and*
885 *Engineering*, *2017*, 1–8. doi:10.1155/2017/4967913
- 886 Yuan-Hui, L. & Gregory, S. (1974), Diffusion of ions in sea water and in deep-sea sediments.
887 *Geochimica et Cosmochimica Acta*, *38*(5), 703–714. doi:10.1016/0016-7037(74)90145-8